Manuscript

Validation study of static and dynamic tsunami source models using the discontinuous Galerkin method for the spherical shallow water equations

Mahya Hajihassanpour[a,b], Boris Bonev[a,*], Jan S. Hesthaven[a]

[a]École polytechnique fédérale de Lausanne (EPFL), CH-1015 Lausanne, Switzerland
[b]Sharif University of Technology, Tehran, Iran

Abstract

The discontinuous Galerkin method is used to solve the non-linear spherical shallow water equations with Coriolis force. The numerical method is well-balanced and takes wetting/drying into account. The two fold goal of this work is a comparative study of dynamic and static tsunami generation by seabed displacement and the careful validation of the models. The numerical results show that the impact of the choice of seabed displacement model can be significant and that using a static approach may result in inaccurate results. For the validation of the studies, we consider measurements from satellites and buoy networks for the 2011 Tohoku event and the 2004 Sumatra-Andaman tsunami. The results confirm that the method is appropriate for large-scale tsunami simulations and early warning systems.

Keywords: Static and dynamic seabed displacement, Tsunami modeling, Shallow water equations, Well-balanced scheme, Wetting and drying, Discontinuous Galerkin method

1. Introduction

Tsunamis are oceanic gravity waves generated by large sea level surface displacements. Such displacements can be generated by volcanic eruptions [1], landslides [2], asteroid impacts [3] or earthquakes [4]. Tsunamis generated by earthquakes are commonplace and can cause considerable damage to human lives and infrastructures. There are various mathematical models, which can be used to model and predict the dynamics of tsunami waves. Such mathematical models should be able to accurately predict the sea surface displacement, velocity and arrival times of waves reaching the coastline. The resulting inundation area and the overall computational cost can also be of interest. The models can be broadly classified as follows:

- 3D models: The governing equations are derived without integrating over the depth. These are non-hydrostatic models, for instance the Navier-Stokes or Euler equations. Although these are accurate models, their computational cost is substantial and currently not applicable to large scale predictive problems [5-7].
- 2D models: These models are derived by integrating over the depth and can be either non-hydrostatic (Boussinesq-type equations) [8,9] or hydrostatic (shallow water equations) [10,11].

Typically, the 3D models are more accurate than the 2D models such as the shallow water equations, but their computational cost make them impractical for the purpose of tsunami predictions. Therefore, we consider the shallow water equations here. The computational cost and accuracy of the tsunami simulations not only depend on the mathematical model but also on the numerical method being applied. In the context of tsunami simulations various methods have been applied. Among them are the finite difference (FD) [12,13], finite volume (FV) [14,15], Finite element (FE) [16], discontinuous Galerkin (DG) [4, 17-20] and hybrid [21,22] methods. While all of these methods have their strengths and weaknesses, the discontinuous Galerkin method stands out in the context of wave problems as it offers high accuracy and efficiency through h/p adaptivity and parallelity.

---

[*] Corresponding author.
 E-mail address: boris.bonev@epfl.ch.

The effects of the earthquake and the subsequent seabed displacement enter the shallow water equations as a source term. This source term can be time-independent (the passive/static approach) [23-26] or time-dependent (the active/dynamic approach) [26-33]. In the static approach, only the final deformation of the seabed is considered. This displacement is introduced into the simulation by displacing the initial sea surface according to the deformation of the seabed. Several assumptions are made in this static approach. First of all, the wavelengths of the tsunami waves are assumed to be much larger than the depth of the ocean. The vertical acceleration of the water is neglected as it is small in comparison to the gravitational acceleration on the water mass that is lifted, which causes a uniform velocity profile in the horizontal direction. Secondly, the vertical seabed displacement is assumed to be instantaneous. This is accurate if the timescale of the earthquake rupture is much smaller than the timescale of the tsunami propagation. Lastly, the horizontal displacement of the seabed is usually neglected, unless the horizontal displacement is large relative to the vertical displacement. The static approach can consist of a single fault [23,24] or multiple faults [25,26]. The multi-fault case can be used to increase the resolution of the seabed displacement due to an underwater earthquake relative to the single-fault. In contrast to the static approach, in the dynamic approach, the full transient motion of the seabed displacement due to an underwater earthquake is considered. The transient seabed displacement can be obtained by considering a simple time function for temporal changes [26-30], recovering an initial condition from buoy data [18], a quasi real-time fault model [31] or solving the equations of elasticity [32,33]. Similar to the static approach, the dynamic approach can be modeled as single-fault [27] or multi-fault [26,28-30].

In recent years, the DG method has been applied to perform tsunami simulations. Seny et al. [19] showed a parallel implementation of an explicit multirate Runge-Kutta discontinuous Galerkin method and applied it to simulate the 2011 Tohoku tsunami. However, they did not consider inundation and the curvature of the sphere and used a static, single-fault seabed displacement model. Blaise et al. [17] considered a simulation of the February 2010 Chilean tsunami using a dynamic hp-adaptive DG method on the sphere. Moreover, they have solved the spherical shallow water equations with Coriolis force in three dimensions using a Lagrange multiplier. However, they too, did not consider inundation. In a later work [18], initial conditions for the Tohoku tsunami were inferred from buoy measurements using a discrete adjoint method, but without taking wetting/drying into account. Castro et al. [20] simulated the April 1, 2014, Iquique event with a static single-fault rupture model. They considered the linearized shallow water equation in two-dimensional Cartesian coordinates without Coriolis force and inundation and used the Arbitrary accurate Derivatives Riemann problem (ADER) DG method with parallel computing on GPUs and CPUs.

In this work, the spherical shallow water equations with Coriolis force is solved in Cartesian coordinates using the method presented in [4]. The method employs curved elements with dynamic mesh refinement. Moreover, the wetting/drying method presented in [4] handles dry areas. To validate the method, simulations of the 2011 Tohoku and 2004 Sumatra-Andaman tsunamis are considered using both dynamic and static seabed deformation. One of the purposes of this work is to investigate the effect of the dynamic seabed displacement on the accuracy of the numerical results. Moreover, we wish to validate the accuracy of the method [4] for tsunami modeling.

The paper is organized as follows: In Section 2, we discuss the governing equations. Section 3, gives an overview of the numerical method [4], comprising the spatial discretization, the time integration, the wetting/drying method, as well as the well-balanced and positivity preserving properties. In Section 4, we discuss the source models that model the generation of tsunamis through an underwater earthquake. This includes the discussion of static and dynamic seabed displacement approaches. In Section 5 we investigate the impact of the static and dynamic approaches on the numerical results. To this end, the 2011 Tohoku and 2004 Andaman-Sumatra tsunamis are investigated. We compare results to measurements to assess their accuracy. Finally, we state our conclusion in Section 6.

2. Governing equations

We consider the spherical shallow water equations as presented in [34], formulated in Cartesian coordinates, and written as a system of conservation laws

$$\frac{\partial \boldsymbol{q}}{\partial t} + \boldsymbol{\nabla} \cdot \boldsymbol{F} = \boldsymbol{S} \tag{1}$$

where $\boldsymbol{q}$, $\boldsymbol{F} = \boldsymbol{f}_x \hat{\imath} + \boldsymbol{f}_y \hat{\jmath} + \boldsymbol{f}_z \hat{\boldsymbol{k}}$ and $\boldsymbol{S}$ are the solution, the flux and the source vectors, respectively. These are given as

$$\boldsymbol{q} = \begin{bmatrix} \varphi \\ \varphi u \\ \varphi v \\ \varphi w \end{bmatrix}, \qquad \boldsymbol{f}_x = \begin{bmatrix} \varphi u \\ \varphi u^2 + \dfrac{\varphi^2}{2} \\ \varphi u v \\ \varphi u w \end{bmatrix}, \qquad \boldsymbol{f}_y = \begin{bmatrix} \varphi v \\ \varphi u v \\ \varphi v^2 + \dfrac{\varphi^2}{2} \\ \varphi v w \end{bmatrix}, \qquad \boldsymbol{f}_z = \begin{bmatrix} \varphi w \\ \varphi u w \\ \varphi u w \\ \varphi w^2 + \dfrac{\varphi^2}{2} \end{bmatrix}, \qquad \boldsymbol{S} = \begin{bmatrix} 0 \\ \tilde{\boldsymbol{S}} \end{bmatrix} \tag{2}$$

where $\boldsymbol{u} = \{u, v, w\}^T$ is the velocity vector and $\hat{\imath}, \hat{\jmath}$ and $\hat{k}$ are the unit vectors in the Cartesian coordinates $\boldsymbol{x} = \{x, y, z\}^T$. Here, $\varphi = gh$ denotes the geopotential height, where g and h are the gravitational acceleration and the water column height, respectively. The source term acts only on the momentum equations, and consists of

$$\tilde{\boldsymbol{S}} = -\frac{2\omega z\varphi}{R^2}\boldsymbol{x} \times \boldsymbol{u} - \varphi\boldsymbol{\nabla}\tau + \mu\boldsymbol{x}. \tag{3}$$

The first term in (3) is the Coriolis force, the second one is the pressure gradient due to the bathymetry and the last term forces the velocity vector be tangential to the spherical shell, i.e., $\boldsymbol{u}.\boldsymbol{x} = \boldsymbol{0}$. The angular velocity of the sphere $\boldsymbol{\omega}$ is defined based on the rotation around the z-axis, where R is the radius of the earth. The bottom topography $\tau = gb$ is measured in geopotential units where b is the bathymetry relative to the sea level. The Lagrange multiplier μ is defined as

$$\mu = \frac{1}{R^2}\boldsymbol{x}.\left(\varphi\boldsymbol{\nabla}\tau + \boldsymbol{\nabla}.\tilde{\boldsymbol{F}}\right) \tag{4}$$

where $\tilde{\boldsymbol{F}}$ is the part of the flux that acts on the momentum equations.

3. Numerical method

The governing equations in the previous section are solved using the numerical method discussed in detail in [4]. We give a short overview of the method and refer the reader for details to [4]. The computational domain Ω with boundary $\partial\Omega$, is divided into K non-overlapping elements. As Ω is the two-dimensional sphere with radius R, elements are curved quadrilaterals of arbitrary sizes and we denote them as D^k. Thus, Ω is the union of D^k, i.e.,

$$\Omega = \bigcup_{k=1}^{K} D^k. \tag{5}$$

To make the computations easier, the mapping $\boldsymbol{\xi} = \psi(\boldsymbol{x})$ is used to transform coordinates from the physical space $\boldsymbol{x} = \{x, y, z\}^T$ to the reference domain $\boldsymbol{\xi} = \{\xi, \eta\}^T$. The numerical solution $\boldsymbol{q}_N$ is expressed as piecewise polynomials

$$\boldsymbol{q} \approx \boldsymbol{q}_N = \bigoplus_{k=1}^{K} \boldsymbol{q}_N^k \tag{6}$$

where $\boldsymbol{q}_N^k$ can be expressed as a linear combination

$$\boldsymbol{q}_N^k(\boldsymbol{x}, t) = \sum_{m=1}^{(N+1)^2} \boldsymbol{q}_N^k(\boldsymbol{x}(\boldsymbol{\xi}_m), t)\, L_m\big(\boldsymbol{\xi}(\boldsymbol{x})\big) \tag{7}$$

of the basis functions L_m which are formed using the tensor-product

$$L_m(\boldsymbol{\xi}) = l_i(\xi)l_j(\eta) \tag{8}$$

of the one-dimensional Lagrange polynomials

$$l_i(\xi) = \prod_{\substack{j=1 \\ j \neq i}}^{N+1} \frac{\xi - \xi_j}{\xi_i - \xi_j}. \tag{9}$$

These polynomials have the nodal property $l_i(\xi_j) = \delta_{ij}$ where δ_{ij} is the Kronecker delta. The nodes ξ_j are chosen to be the Legendre-Gauss-Lobatto (LGL) nodes, which are defined on the interval $[-1,1]$. As a consequence, the reference element in computational space is $I = [-1,1]^2$. Applying the weighted residual method to the governing equations (1), yields

$$\int_D \left(\frac{\partial \boldsymbol{q}}{\partial t} + \boldsymbol{\nabla}.\boldsymbol{F} - \boldsymbol{S}\right)\phi(\boldsymbol{x})\, d\boldsymbol{x} = \int_I \left(\frac{\partial \boldsymbol{q}}{\partial t} + \boldsymbol{\nabla}.\boldsymbol{F} - \boldsymbol{S}\right)\phi(\boldsymbol{\xi})\, J_D\, d\boldsymbol{\xi} = 0 \tag{10}$$

where ϕ is a test function. To derive the nodal version of the discontinuous Galerkin method, the test and shape functions are set equal to each other, thus $\phi_m = L_m$. The strong form of the nodal discontinuous Galerkin method is recovered as

$$\int_I \left(\frac{\partial \boldsymbol{q}_N}{\partial t} + \boldsymbol{\nabla}.\boldsymbol{F}_N - \boldsymbol{S}_N\right) L_i J_D d\boldsymbol{\xi} = -\oint_{\partial I} \hat{\boldsymbol{n}}.\left(\boldsymbol{F}_N - \boldsymbol{F}_N^*\right) L_i J_{\partial D} d\boldsymbol{\xi} \tag{11}$$

where $\hat{n}$, J_D and $J_{\partial D}$ are the outward unit normal to the edge of element, the Jacobian of the element and the Jacobian of the edge parametrization, respectively. Due to the discontinuous nature of the solution, a suitable numerical flux $\boldsymbol{F}^*$ must be defined to connect the solution across interfaces. We use the local Lax-Friedrichs numerical flux

$$F_N^* = \frac{1}{2}\left(F_N^*(q_N^-) + F_N^*(q_N^+) \right) - \frac{c}{2}\left(q_N^+ - q_N^- \right) \tag{12}$$

where the superscripts $-$ and $+$ refer to values within the element and neighboring element, respectively. The factor c is the maximum local wave speed across the element boundary, given as

$$c = \max\left\{ |\hat{n}.u_N^-| + \sqrt{\varphi_N^-}, \ \ |\hat{n}.u_N^+| + \sqrt{\varphi_N^+} \right\}. \tag{13}$$

Finally, to complete the numerical scheme, the integrals in (11) have to be computed numerically. To this end, quadrature rules for the approximation of the volume and the surface integral terms are used. Thus, we obtain a system of ordinary differential equations in the form of

$$\frac{\partial q_N}{\partial t} = R_N(q_N), \tag{14}$$

where R_N is the right-hand side obtained by applying the quadrature rules in the discontinuous Galerkin formulation. Here, a three-step, third-order strong stability preserving Runge-Kutta method is used to solve this semi-discrete form [35].

In order to take care of inundation, we follow the method described in [4]. We call a node x_i dry if the water height $\varphi_N(x_i)$ is smaller than a certain tolerance φ_{tol}. We distinguish between wet, dry and semi-dry elements. The latter contains both wet and dry nodes, which poses difficulties in the numerical treatment of these elements. More specially, these are the appearance of negative water heights, artificial pressure gradients and instabilities due to the discontinuity in the derivative of the state variables. To guarantee the positivity of the water column height, we use the method presented in [36]. Well-balancedness is then guaranteed by using a finite-difference type gradient operator only in the semi-dry elements, which prevents the occurrence of artificial pressure gradients [4]. Moreover, a filter is used to address stability issues. N-conforming meshes are handled in the same way as in [4].

4. Tsunami generation

For the static seabed displacement approach we assume that fault parameters such as the longitude (Lon), latitude (Lat), depth, length, width, strike, dip, rake and slip are known. Using these parameters, the Okada solution can be computed [37], to recover the seabed displacement caused by the earthquake thrust. For a dynamic approach, two additional parameters, i.e., the rupture velocity (or the rupture initiation time) and rise times are needed. There is an explicit relation between the rupture velocity and the rupture initiation time. If the rupture velocity is considered to be constant in each subfault i, then

$$t_0^{i+1} = \frac{l^i}{V^i} + t_0^i, \quad i = 1,2,\ldots,N_f \tag{15}$$

where l^i, V^i, t_0^i are the length, rupture velocity, rupture initiation time of the i-th subfault and N_f the total number of subfaults. Here we assume that $t_0^1 = 0$.

If a fault has been divided into N_f subfaults, then the total displacement of the seabed can be considered as the sum of displacements for each subfault, i.e.,

$$\zeta(x) = \sum_{i=1}^{N} O^i\left(x^i, l^i, w^i, d^i, \ldots \right) \tag{16}$$

where O^i is the Okada solution in the i-th subfault. Note that the Okada solution computes a static seabed displacement. Thus, to achieve a dynamic rupture model, a time-activation function f^i is considered for each subfault. In other words (16) is modified as

$$\zeta(x,t) = \sum_{i=1}^{N} f^i(t,t_0^i,t_0^{i+1}) \, O^i\left(x^i, l^i, w^i, d^i, \ldots \right), \tag{17}$$

where different activation functions $f^i(t,t_0^i,t_0^{i+1})$ can be used [28, 29, 38]. Here, a linear activation function [28] is used:

$$f^i\left(t, t_0^i, t_0^{i+1} \right) = \begin{cases} 0 & \text{if } t < t_0^i \\ \dfrac{t - t_0^i}{t_0^{i+1} - t_0^i} & \text{if } t_0^i \le t \le t_0^{i+1} \\ 1 & \text{if } t_0^{i+1} < t \end{cases}. \tag{18}$$

5. Numerical Results

In the following, we present numerical results with the aforementioned implementation of the discontinuous Galerkin method (DGM) for the spherical shallow water equations. To understand the effects of the static and dynamic seabed displacement approaches on the tsunami waves, we compare the two models using two different tsunami events. These two tsunamis are the 2011 Tohoku and the 2004 Andaman-Sumatra events. The numerical results obtained for these two tsunamis are compared with the available measured data to validate the numerical model. These two tsunamis are chosen as they are the two largest and most devastating events in recent decades, with plenty of data available. Moreover, their character is quite different as the earthquake that caused them have vastly differing fault dimension and rupture speeds.

5.1. Tohoku event

On March 11th, 2011, at 2:46 pm JST (05:46 UTC) a massive earthquake of magnitude $M_w = 9.0$ struck near the northeastern coast of Japan, resulting in massive seafloor displacement and high tsunami waves. The first significant waves reached Japan only 10 min after the earthquake struck, thus leaving very little warning time. This tsunami caused thousands of fatalities and financial damage of hundreds of billion dollars. The characteristics of this tsunami make it interesting for assessment and validation of the numerical method.
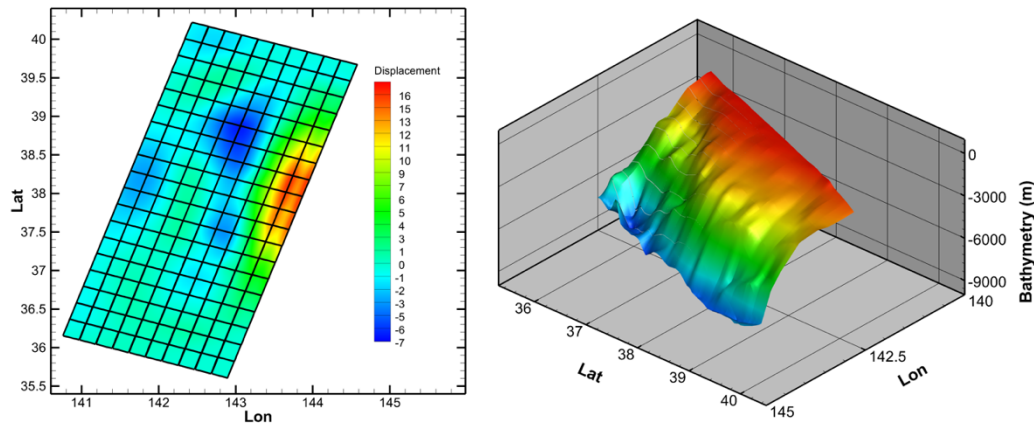

Figure 1: Left: subfaults and the seabed displacement for the Tohoku earthquake and Right: bathymetry in the corresponding subfaults.

To obtain the seabed displacement using the Okada model [37], subfault parameters are taken from the University of California, Santa Barbara (UCSB) database for big earthquakes [39]. We use the parameters of model III presented in [39]. These parameters include both static and dynamic parameters. In the aforementioned data, the number of subfaults in the strike direction is 19 and in down-dip direction 10, which results in the total numer of $N_f = 190$ subfaults. The length of each subfault in the strike direction is 25 km whereas it is 20 km in the down-dip direction. The fault is situated between 35.74° and 40.09° northern latitude and between 140.91° and 144.42° eastern longitude. By inserting the fault parameters into (16), the final displacement of the seabed, which is shown in Fig. 1, is obtained. As shown in this figure, the maximum lift of the seabed is located on the eastern side of the fault. The bathymetry within the subfaults is illustrated in Fig. 1. Apart from the initial displacement, an accurate simulation requires accurate bathymetry data. Note that if the earthquake makes the topography shallower or deeper, both the near-field and the far-field solutions can be affected, as this would change the wave speed in the vicinity. Here, the maximum lift of the seabed is in an area where the water is relatively deep, so the ratio between the maximum lift and the water depth is small. The dynamic rupture can be modeled by (18). The seabed displacement as a function of time is illustrated in Fig. 2. As shown in this figure, the seabed is relatively stable after 105 seconds.
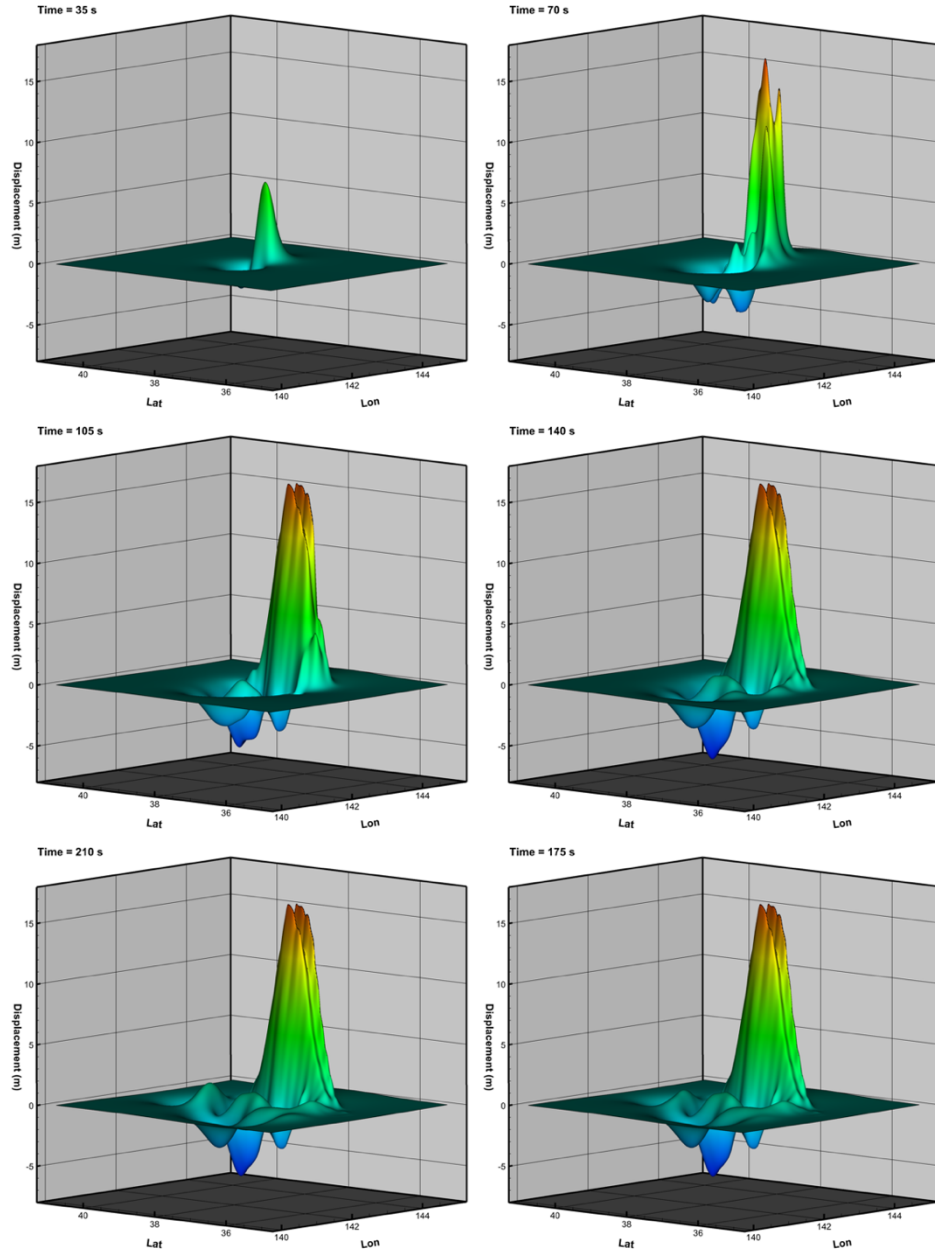
Figure 2: Seabed displacement caused by the Tohoku earthquake at different times

The mesh generated for the Tohoku tsunami event is shown in Fig. 3. The initial mesh is an unrefined icosahedral mesh. A point at -177° longitude and 12° latitude is selected to refine the initial grid within a radius of 55° until a local refinement level of $N_{loc} = 5$ is reached. The resulting mesh contains 14235 elements, of which most are located in the Pacific Ocean. As shown in Fig. 3, the generated mesh is considerably coarser on the opposite side of the sphere. Using this approach for grid generation, regions of interest can be refined locally and the computational cost is decreased dramatically.
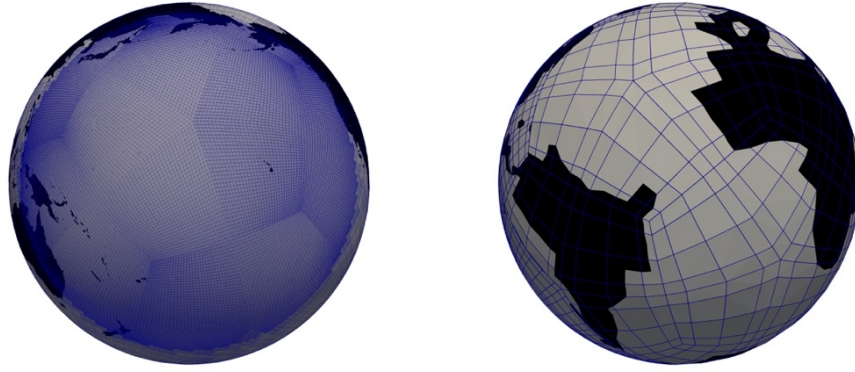
Figure 3: Mesh generated for the simulation of the Tohoku tsunami.

The propagation of the tsunami waves is shown at different times in Fig. 4. In this figure, we show the results obtained with the static seabed displacement approach and biquartic polynomials $N = 4$. As is clear, at initial time, the seabed displacement has been transferred to the water height. After a while, tsunami waves propagate into the Pacific Ocean and their amplitudes diminish.

Differences between the static and dynamic approaches are shown in Fig. 5. In this figure, numerical results obtained with the static approach are denoted by h_s and for the dynamic approach are denoted by h_d. In the left column of the figure the contour levels between -0.1m and 0.1m while in the right column of the figure we show the contour levels between -1m and 1m. Results presented in the right column show that differences between the two seabed displacement models are small when big waves are considered. It is clear that big waves affect a small zone in the Pacific Ocean. However if small differences are considered, as shown in the left column, then the differences between results are significant even in the far-field. Therefore, an important factor in choosing the seabed displacement approach is whether the result needs to be accurate and where the zone of interest lies with respect to the tsunami source. If the zone of interest is located near the earthquake zone or if high accuracy is needed then the dynamic approach should be considered.

The results presented in Fig. 5 are qualitative results. It is more valuable to present quantitative results. For this, results obtained by the DG method are compared with buoy data. These buoys are the DART buoys 21418 and 52402. The buoy data is collected by the DART tsunami monitoring network and are provided online by the National Data Buoy Center (NDBC) of the National Oceanic and Atmospheric Administration (NOAA) [40]. By subtracting the time-average from the buoy data, we eliminate the effect of tides, which are not considered in our model.

Here, we have performed numerical simulations using two polynomial degrees, $N = 2$ and $N = 4$ to validate our model and to understand effects of the polynomial degree on the numerical results. It is expected that using higher degree polynomials result in higher accuracy. For the buoy 21418, effects of the polynomial degree are shown in Fig. 6. As shown in this figure, using biquartic polynomials results in a higher accuracy compared to the results obtained with biquadratic polynomials. It is also clear that the biquartic polynomials capture the maximum water height more accurately than the biquadratic polynomials. This is expected as higher order methods are less dissipative and therefore better suited for large scale solutions where the solution is smooth in large parts of the domain. The same comparison is also conducted for the buoy 52402 in Fig. 7. The situation is similar to buoy 21418, and we observe that the agreement with the buoy data, for instance the arrival time, is satisfactory. For both the static and dynamic seabed displacement approaches, using $N = 4$ results in more accurate results than $N = 2$. These results show that the developed DG method can be used for tsunami simulations.

The comparison of the static and dynamic seabed displacement approaches is presented in Fig. 8. The differences are not significant and there is only a slight advantage of the dynamic seabed displacement approach, which leads to better agreement in the buoy data. We observe that for both buoys, the predicted arrival times are in better agreement

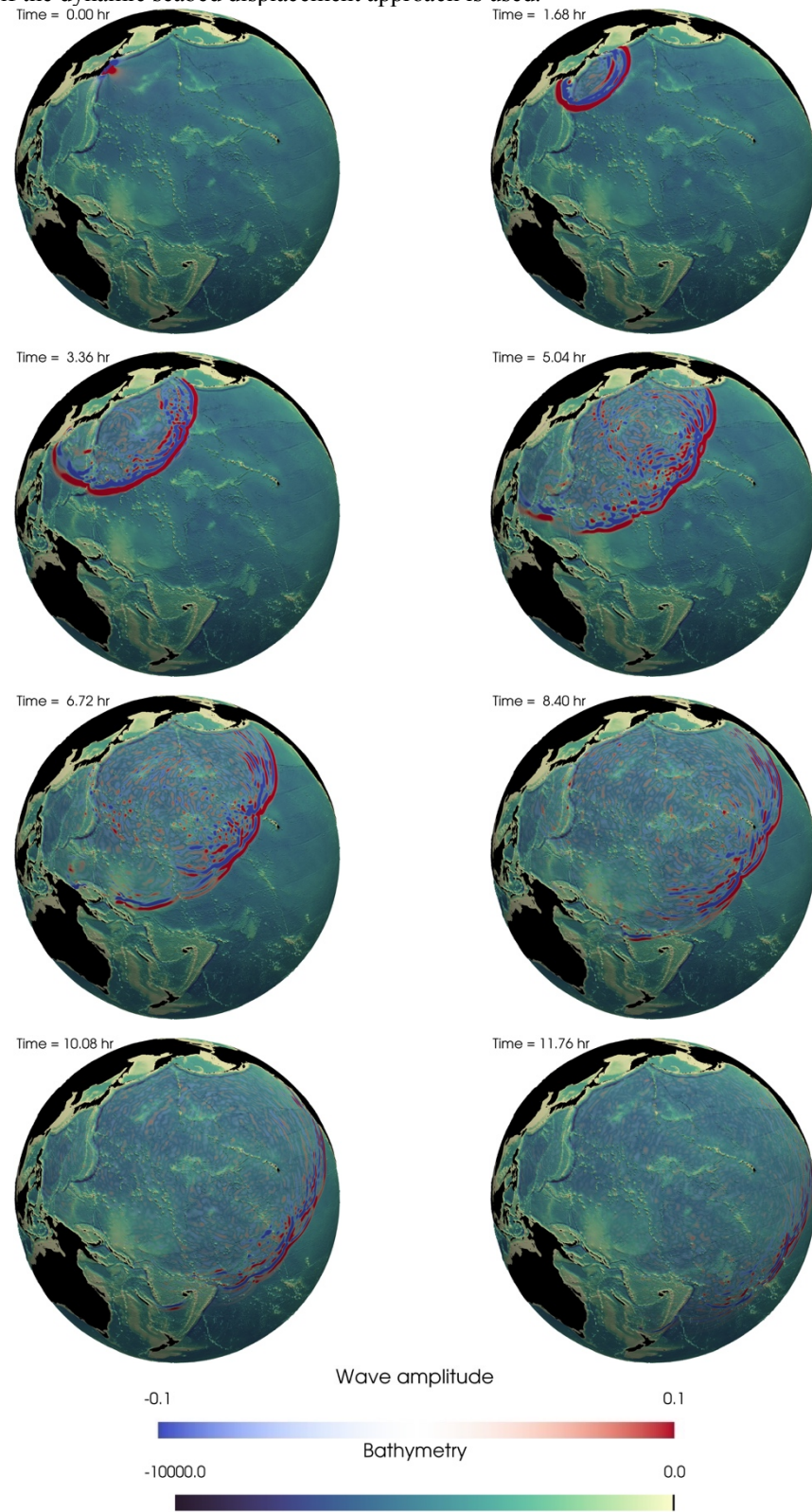with the buoy data if the dynamic seabed displacement approach is used.

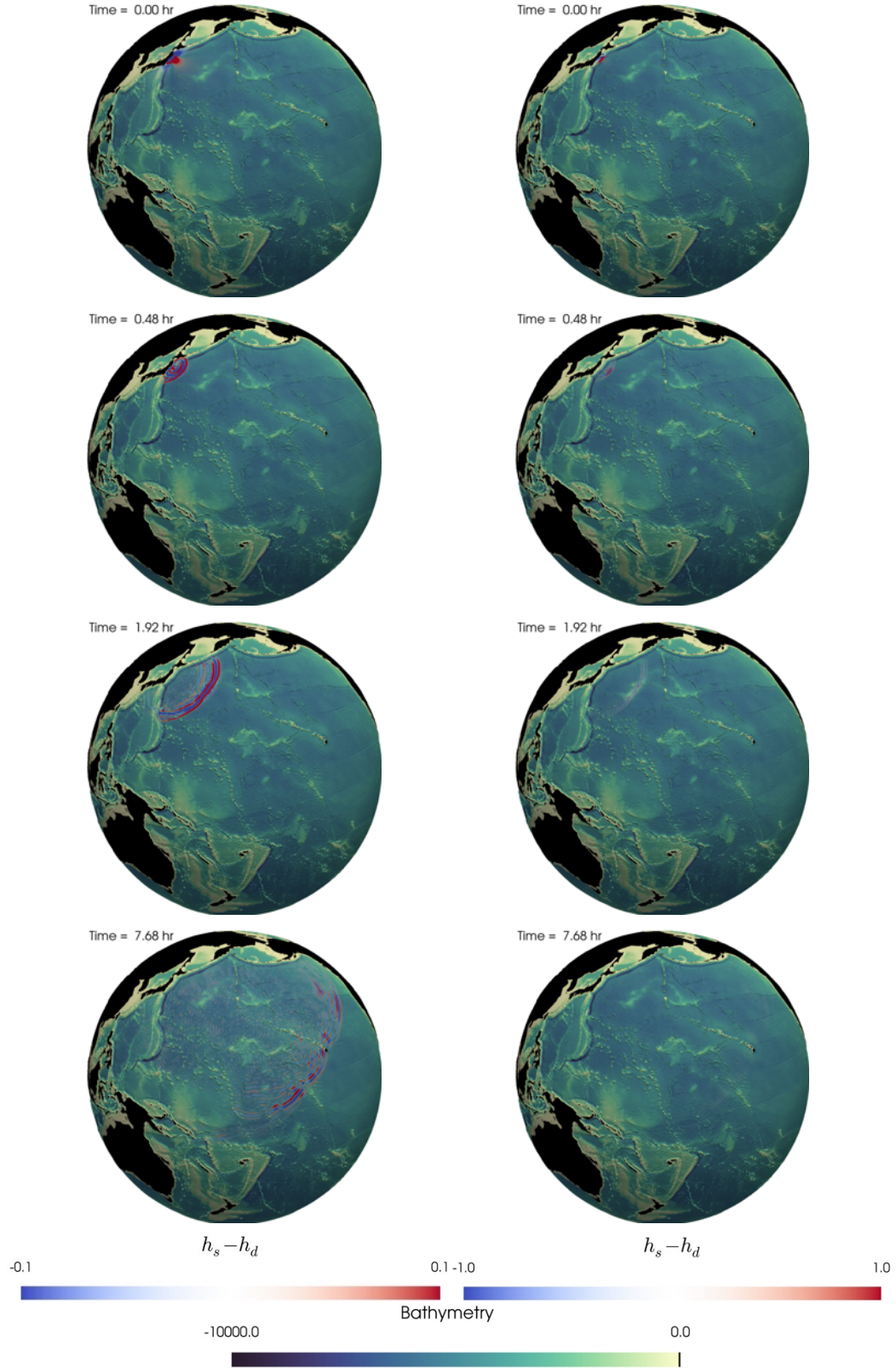Figure 4: Simulation of tsunami waves created by the Tohoku earthquake

Figure 5: Differences in wave amplitude between static and dynamic seabed deformations. The left column depicts contour lines between -0.1m and 0.1m, the right column depicts differences between -1m and 1m.
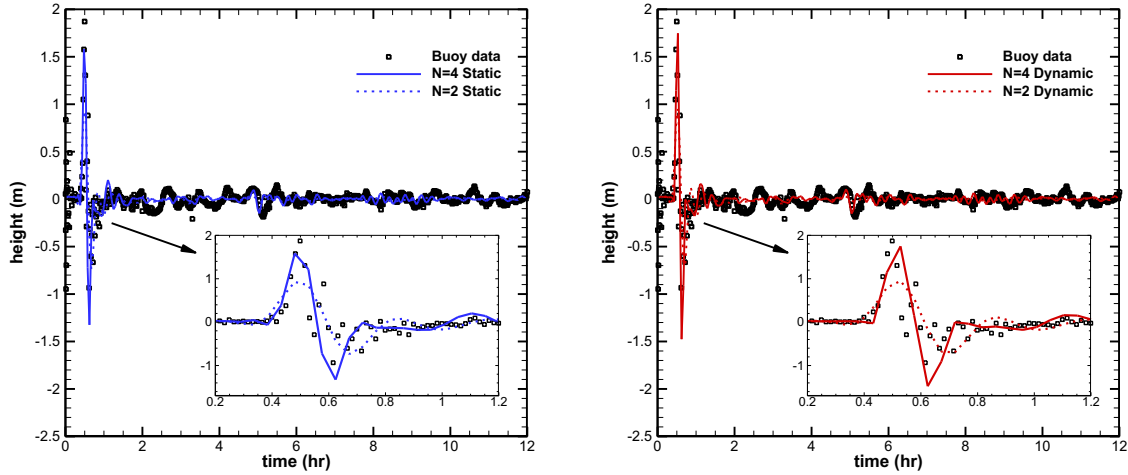
Figure 6: Effect of the polynomial degree on the computed sea surface height in comparison to the DART 21418 buoy measurements. Left: sea surface heights computed with static seabed deformation. Right: sea surface heights computed with dynamic seabed deformation.
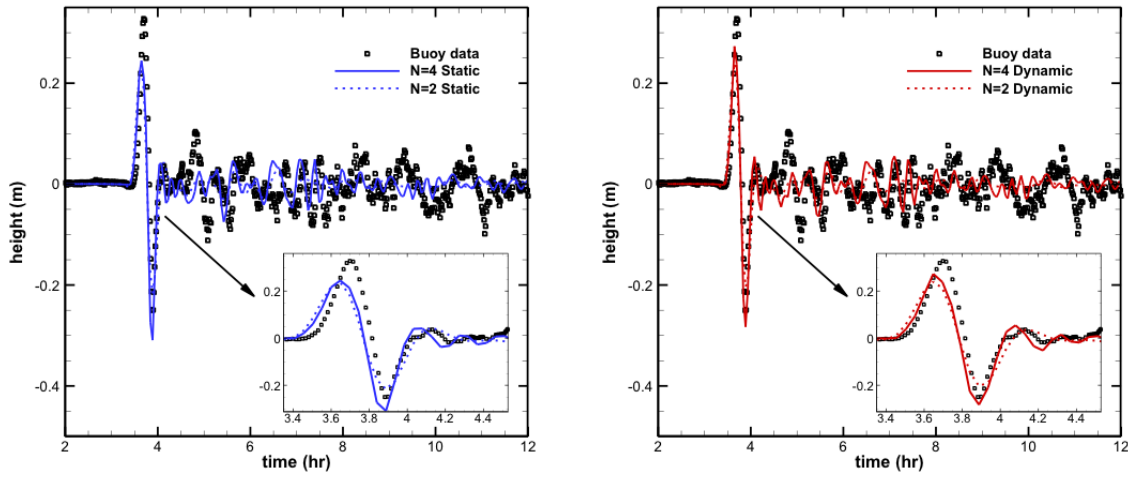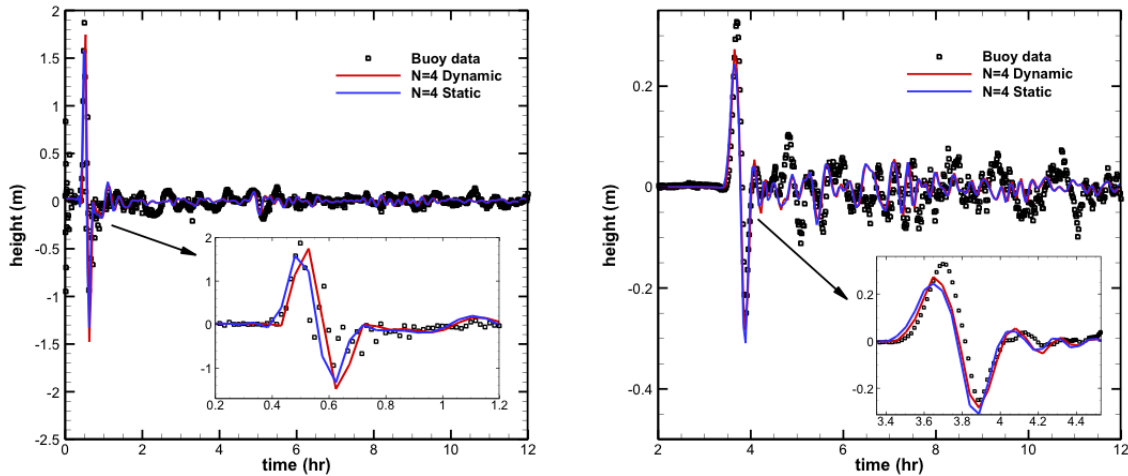

Figure 7: Effect of the polynomial degree on the computed sea surface height in comparison to the DART 52402 buoy measurements. Left: sea surface heights computed with static seabed deformation. Right: sea surface heights computed with dynamic seabed deformation.

Figure 8: Comparison of the static and dynamic seabed deformation approaches using buoy data. Left: DART 21418 Right: DART 52402
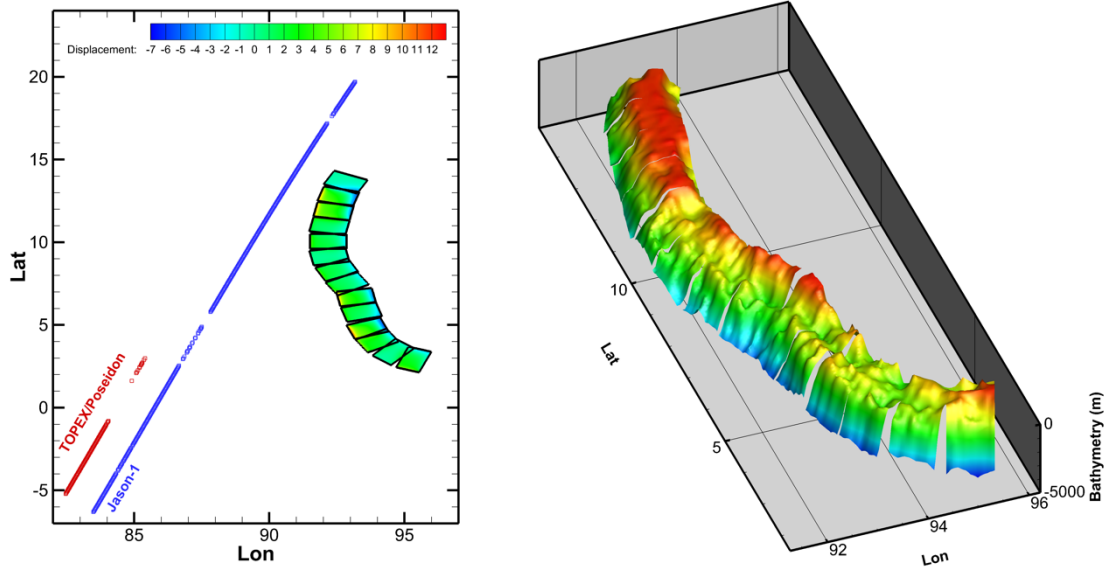
5.2. Sumatra-Andaman event

Figure 9: Left: Subfaults and seabed displacement of the Sumatra-Andaman earthquake. Satellite measurements from Jason-1 and TOPEX/Poseidon are indicated in the figure. Right: Bathymetry in the corresponding subfaults.

On December 26th, 2004, at 0:59 AM UTC an earthquake of magnitude $M_w = 9.1 - 9.3$ struck near the west coast of Sumatra, Indonesia, resulting in tsunami waves which affected many surrounding nations. It is the third-largest earthquake ever recorded on a seismograph and has the longest ever recorded fault duration of about 10 minutes. This tsunami caused hundreds of thousands of fatalities and financial damage of hundreds of billion dollars. It's large fault size and the long fault duration as well as it's destructive power make it an appropriate, yet challenging test scenario to compare the static and dynamic seabed displacement models.

Table 1: Earthquake parameters used for the simulation of the Sumatra-Andaman tsunami.

subfaults	Lon	Lat	Depth	Length	Width	Strike	Dip	Rake	Slip	Initiation time	Rise time
1	95.54	2.13	10	100	150	290	10	71	16.5	0	48.5
2	94.5	2.57	10	100	150	310	10	91	0	31.96	48.5
3	93.64	3.33	10	100	150	330	10	104	14.9	136.85	37.5
4	93.16	4.15	10	100	150	340	10	105	29.1	167.62	117.3
5	92.88	5.18	10	100	150	345	10	102	10.4	227.09	138.7
6	92.63	6.12	10	100	150	350	10	100	23.4	254.98	62.1
7	92.53	6.78	10	100	150	330	10	90	9.4	282.41	38.5
8	92.08	7.64	10	100	150	335	10	86	11.5	308.57	111.2
9	91.64	8.6	10	100	150	350	10	99	1.5	334.06	63.9
10	91.51	9.6	10	100	150	0	10	106	12	396.16	51.3
11	91.48	10.66	10	100	150	10	10	115	6.1	433.33	79
12	91.63	11.56	10	100	150	10	10	115	25.7	467.73	54.6
13	91.78	12.51	10	100	150	15	10	120	27.2	502.11	76.8
14	92.01	13.51	10	100	150	25	10	130	0	583.82	36.6

Again, subfault parameters are required to calculate the seabed displacement, caused by the earthquake. Since there are uncertainties in the inverted parameters, different earthquake parameters have been proposed in the literature [41-47]. Here, the parameters have been taken from [41]. Moreover, for the dynamic rupture parameters such as rise time and rupture initiation time, we use the data given by Gopinathan et al. [42]. To this end, the velocity rupture and rise times have been taken from Fig. 7 in [42] and the rupture initiation time is calculated by (15). The fault parameters used in this paper are given in Table 1. For this tsunami, the total number of subfaults is $N_f = 14$. The length of the subfaults in the strike direction is 100 km and 150 km in the dip direction. The fault is situated between 2.13° and 13.51° northern latitude and between 91.48° and 95.54° eastern longitude. With the fault parameters given in Table 1, and using the static rupture approach, we use (16) to obtain the displacement shown in Fig. 9. As shown in this figure, the seabed displacement in subfaults 4, 6, 12 and 13 is much larger than the displacement in other subfaults.

Moreover, the figure displays points that are related to Jason-1 and TOPEX/Poseidon satellite data, which will be used to validate the results. The bathymetry in the subfaults is illustrated in Fig. 9. As opposed to the Tohoku earthquake, we observe that the bathymetry at the fault is much shallower. As the wave speed is proportional to the square root of the water depth, nonlinear effects can change the tsunami behavior if the ratio of seabed displacement to bathymetry depth becomes large. These nonlinearities are negligible in deep waters, however they become more important in shallow waters. Note that in both the Tohoku and Sumatra-Andaman tsunamis this ratio is relatively small.
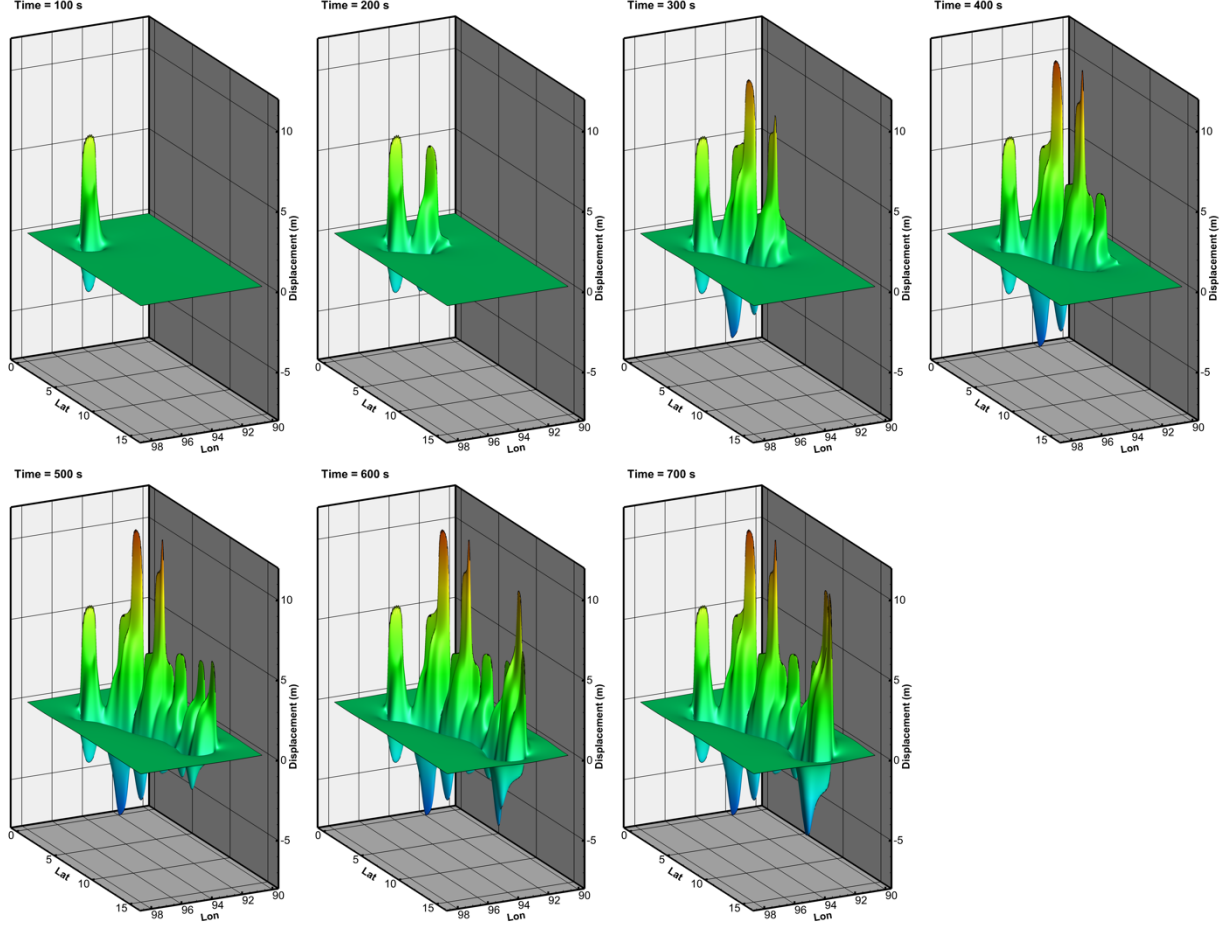
Figure 10: Seabed displacement over time caused by the Sumatra-Andaman earthquake.

The seabed displacement as a function of time can be modeled by (17) and is illustrated in Fig. 10. As shown in this figure, the changes in the seabed are more complex than in the Tohoku case. Not only is the fault very long but also the rupture time is longer than for the Tohoku case. These earthquake characteristics make this problem challenging for tsunami simulation. As depicted in Fig. 10 and also as shown in Table 1, subfaults are activated sequentially. Thus, capturing the transient motion of the seabed displacement is likely to be important.

The mesh generated for the Sumatra-Andaman tsunami event is shown in Fig. 11. Similar to the Tohoku tsunami simulation, the initial mesh is an unrefined icosahedral mesh. A point at 84° longitude and -10° latitude is selected to refine the initial grid within a radius of 40° until a refinement level of $N_{loc} = 6$ is reached. The resulting mesh contains 30378 elements that are located in the Indian Ocean. This mesh has about twice the number of elements compared to the one used in the Tohoku tsunami simulation. There are small islands near the source, so a finer grid in comparison to the Tohoku tsunami simulation is required.
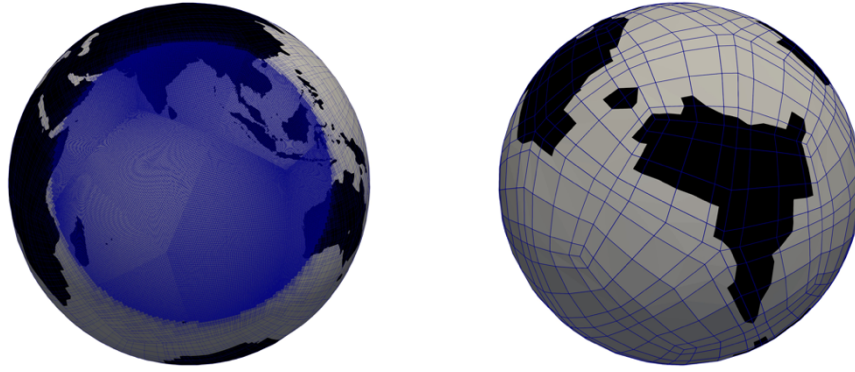
Figure 11: Front and back of the mesh used for the simulation of the Sumatra-Andaman tsunami.

The propagation of the tsunami waves are shown for different times in Fig. 12. In this figure, changes in water height obtained using the static rupture approach and biquartic polynomial $N = 4$ are shown. As illustrated in the figure, the seabed displacement has been translated to the water height at the initial time, since the static (instantaneous) approach is used. After a while, tsunami waves propagate into the Indian Ocean and waves become smaller.

The differences in the numerical results between the static and dynamic displacement models are shown in Fig. 13. The results presented in the right column show that the differences between the models are more prevalent in the near-field of the tsunami source. It can be seen that big waves affect a relatively small area in the vicinity of the source. If we consider the smaller differences, shown in the left column, it is clear that the differences are significant even in the far-field. It is also evident that the dynamic model has a more substantial impact in the case of the Sumatra case. While the large differences between the two models are restricted to a relatively small region in the Tohoku case, this region is much larger for the Sumatra-Andaman tsunami. The use of the dynamic approach can therefore be advantageous even for results in the far-field. Note that for the Tohoku earthquake the major seabed displacements are mostly located on the eastern side of the fault, whereas they are located in all subfaults in the Sumatra-Andaman case. Furthermore, the rupture time of the Sumatra-Andaman earthquake is much longer than that of the Tohoku event, so that differences between the static and dynamic approaches are expected to play a bigger role in the former case.

To validate the use of the DG method, we compare our results to measurements. For the Sumatra-Andaman tsunami there is satellite altimeter data available, which can be used to compute the sea surface height (SSH) along the trajectory of the satellite. Here, we use the data from two satellites namely, Jason-1 and TOPEX/Poseidon, which passed over the Indian Ocean while the tsunami occurred. Jason-1 captured SSHs about 1.9 hours after the earthquake. It passes from south to north and its altimeter measurement is numbered cycle 109 on pass 129. TOPEX/Poseidon captured the SSHs about 2.0 hours after the occurrence of the earthquake. It passes from south to north and its altimeter measurement is numbered cycle 452 on pass 129. The pass of these two satellites and their trajectory relative to the fault is shown in Fig. 9. The altimeter data from these two satellites are available online on the Radar Altimeter Database System web site of the Department of Earth Observation and Space Systems [48]. The measurements of the SSH from satellites does not only include the tsunami signals but also other oceanographic effects [43]. To obtain tsunami signals, the SSH data from previous cycles is used. Therefore, tsunami signals related to Jason-1 are obtained by subtracting measurements of cycles 109 and 108 and for TOPEX/Poseidon, it is obtained by subtracting measurements of cycles 452 and 451. Since the SSH locations in previous cycles may not be the same as those during the tsunami, a linear interpolation is used to estimate the values at the same locations. Here, it is assumed that oceanographic effects are the same in both cycles, so the difference between these two cycles gives the tsunami signals [43]. The satellite data and tsunami signals obtained are shown in Fig. 14.

To understand the effect of the polynomial degree on the numerical results, polynomial degrees of $N = 2$ and $N = 4$ are used in the simulations, and their results are compared with the measurements from Jason-1 satellite in Fig. 15 and measurements from TOPEX/Poseidon satellite in Fig. 16. It is clear that in both cases, the results are accurate and their results are acceptable. Again, the biquartic polynomials are more appropriate than biquadratic ones for large scale simulations, since they have lower numerical dissipation and therefore capture water wave heights in the far-field better. It can be seen from Figs. 15-16 that the DG method can be used to accurately predict tsunami propagation on large scales. It estimates arrival times and maximum wave heights accurately and the numerical results have a satisfactory agreement with the measurements obtained by the satellites.
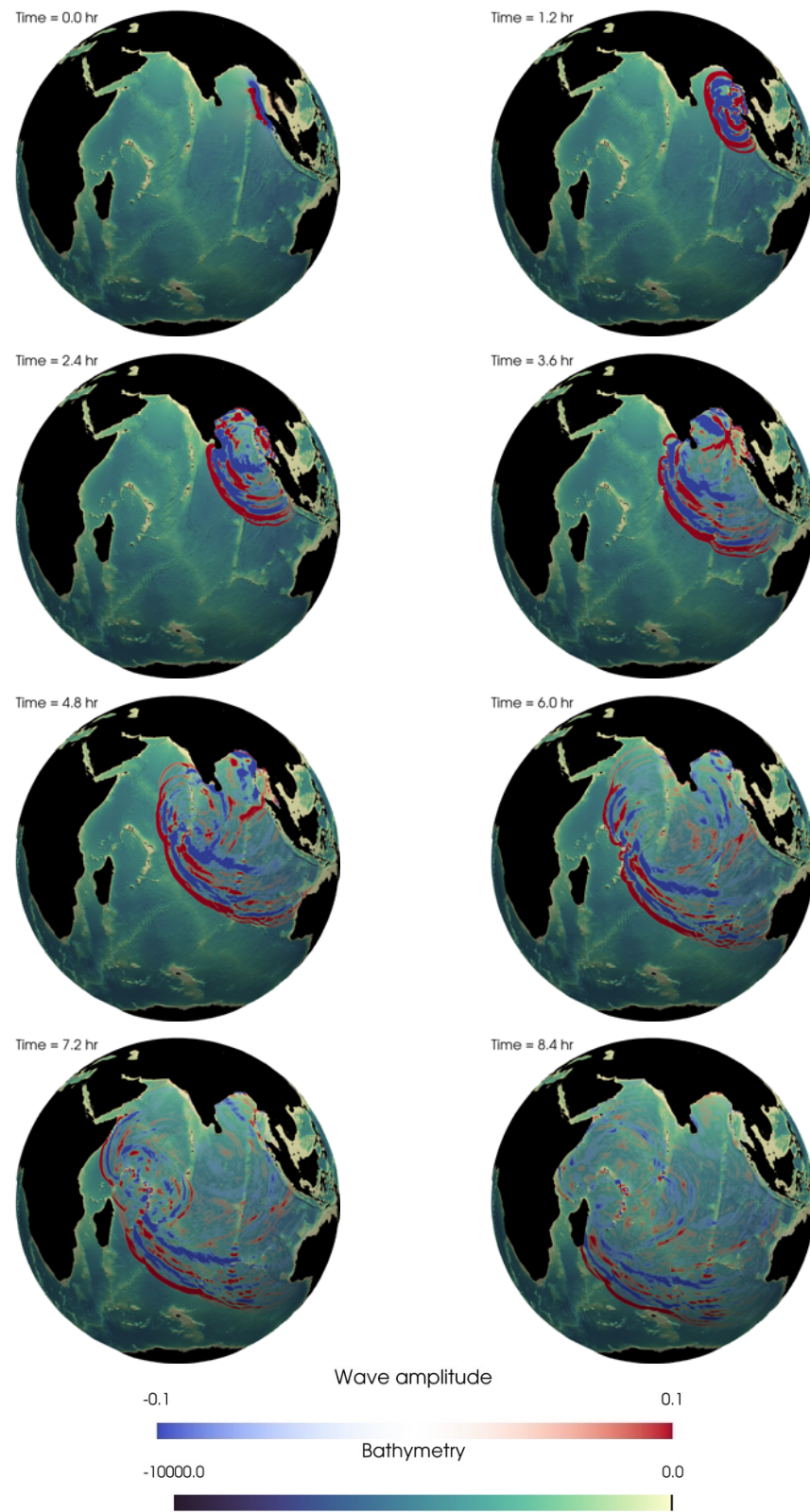
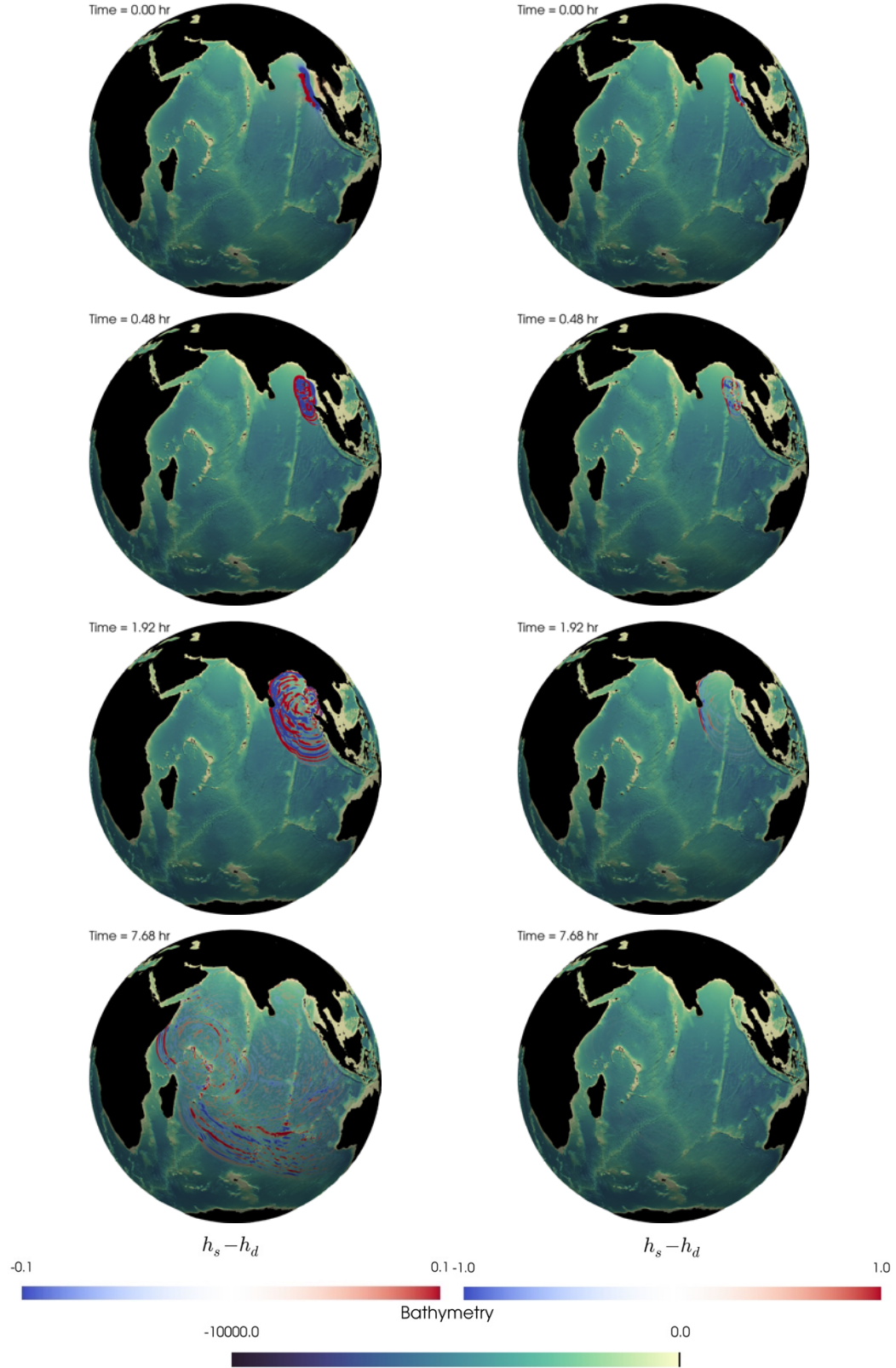Figure 12: Propagation of tsunami waves for the Sumatra-Andaman event.

Figure 13: Differences in wave amplitude between static and dynamic seabed deformations for the Sumatra-Andaman tsunami. The left column highlights small differences between -0.1m and 0.1m while the right column highlights large differences between -1m and 1m.
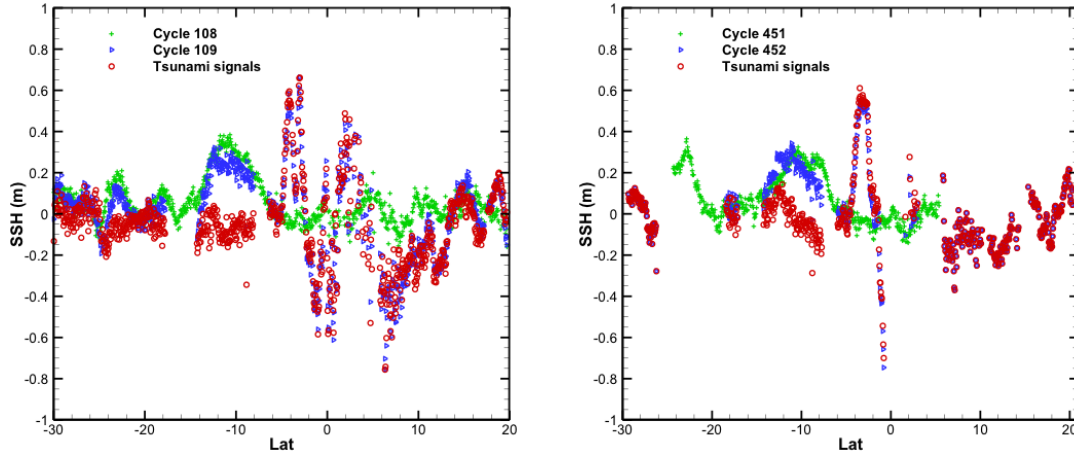
Figure 14: Sea surface level (SSH) measurements from satellite data and extracted tsunami signals. Left: Data obtained from the Jason-1 satellite. Right: Measurements obtained from the TOPEX/Poseidon satellites.
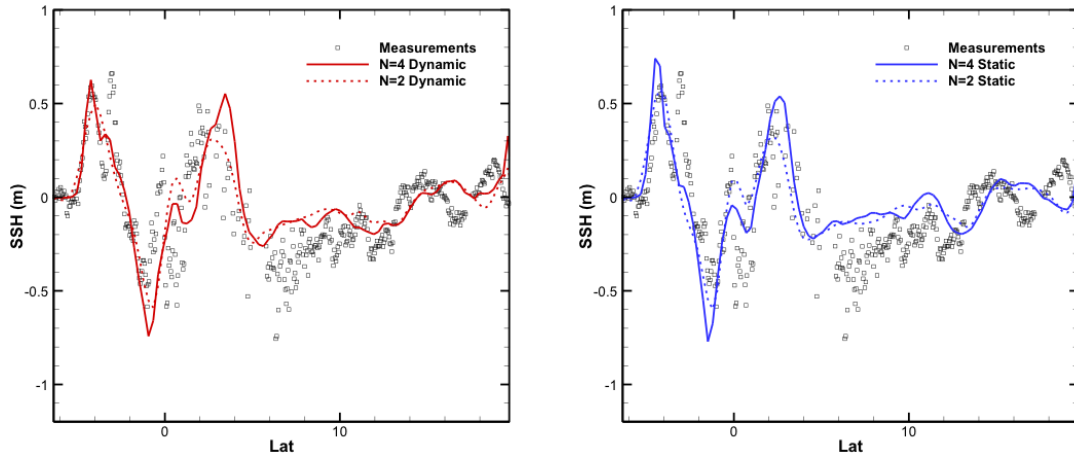

Figure 15: Effect of the polynomial degree on the computed sea surface height and comparison with Jason-1 satellite measurements. Left: Results computed with the dynamic seabed deformation approach. Right: Results computed with the static seabed deformation approach.
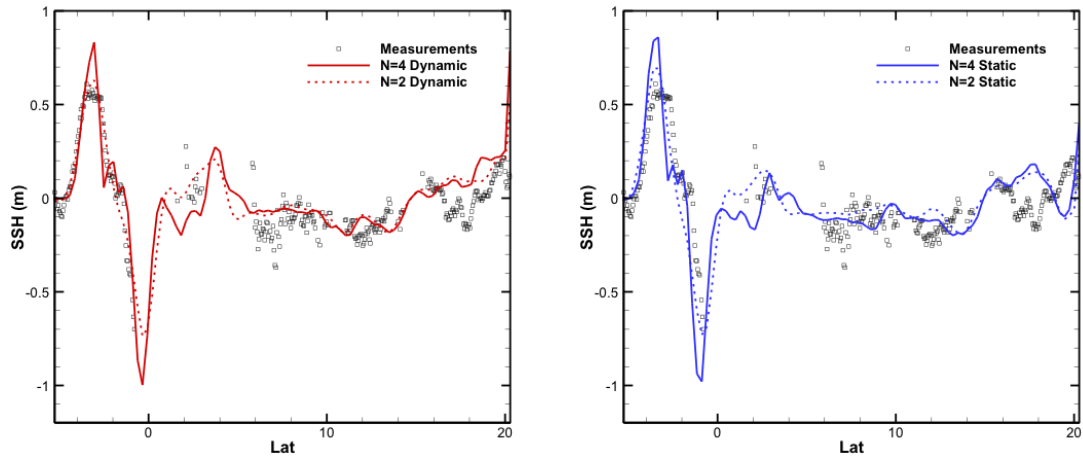

Figure 16: Effect of the polynomial degree on the computed sea surface height and comparison with TOPEX/Poseidon satellite measurements. Left: Results computed with the dynamic seabed deformation approach. Right: Results computed with the static seabed deformation approach.
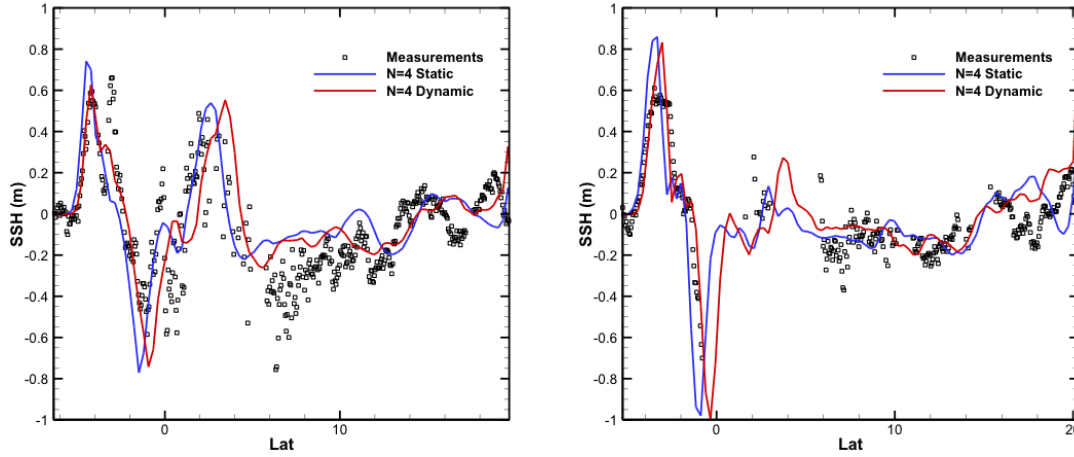
Figure 17: Effect of the seabed deformation approach on the computed sea surface height. Left: Comparison to data ibtained from the Jason-1 satellite. Right: Comparison to data obtained from the TOPEX/Poseidon satellites.
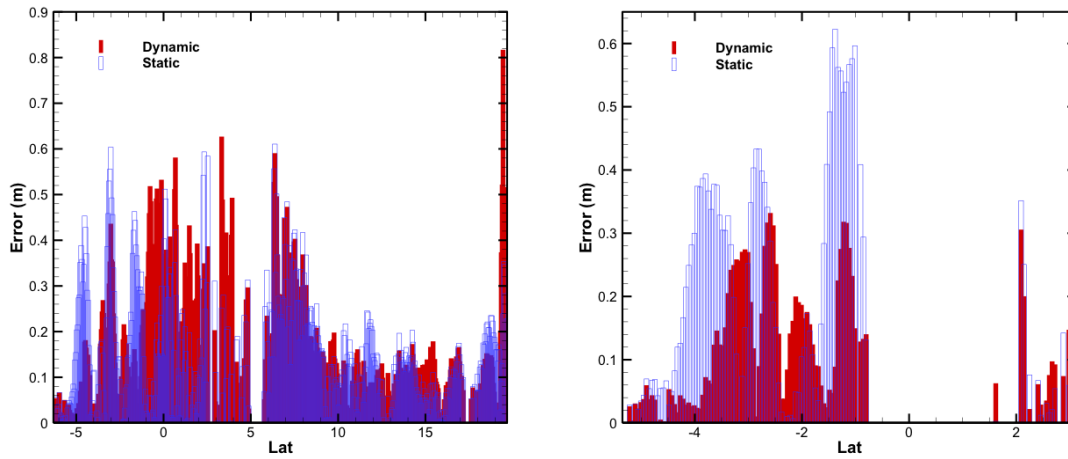

Figure 18: Effect of the seabed deformation method on the error defined by the absolute difference of the computed sea surface height and the measured sea surface height. Left: Errors based on Jason-1 data. Right: Errors based on TOPEX/Poseidon measurements.

The numerical results obtained with the static and dynamic seabed displacement models are compared to the satellite data in Fig. 17. Contrary to the Tohoku case, results obtained for the Sumatra-Andaman tsunami show that there is a substantial difference between the two models. This is clear in Fig. 17, where differences between the static and dynamic approaches are more significant at higher latitudes, whereas in lower latitudes there is a relatively small difference between these two models. The reason is that the southern subfault is activated first and the last one to be activated is the northern subfault. Therefore, for points that are mainly affected by the southern subfault, there is a small difference between both source models, while for points that are affected by the northern subfault, there is a substantial difference between the two approaches. As shown in the figure, the dynamic approach has an advantage to the static approach, as it predicts arrival times and maximum amplitudes of waves with improved accuracy.

In Fig. 18, errors are shown, based on the absolute difference between the numerical results and the satellite measurements. The errors are obtained based on the points in the two sequential cycles of the satellites (see Fig. 14). The corresponding points are also shown in Fig. 9. In other words, points that only exist in one cycle are not considered for evaluating the errors, as they are less reliable. As shown in Fig. 18, the results obtained with the dynamic approach are more accurate. Moreover, the L2-norm of the resulting errors are given in Table 2. For the Jason-1 data, there errors for both models are comparable. For the TOPEX/Poseidon data, however, the dynamic approach has an error of 0.1527, while the error of the static model is 0.2775. This indicates that, indeed, the dynamical approach can provide significantly better numerical results.

Table 2: L2-norm of the errors based on the difference between computed and measured sea surface height.

	Static model	Dynamic model
Jason-1	0.2047	0.2048
TOPEX/Poseidon	0.2775	0.1527

6. Conclusion

In this paper, a discontinuous Galerkin method was applied to model the shallow water equations on the rotating sphere with Coriolis force to simulate two large-scale tsunami events. The DG method uses curved elements and takes wetting/drying into account while also being well-balanced. We use two different approaches to model the initial seabed displacement, caused by the underwater earthquake. These are the static and dynamic displacement models. We compared our method to measurements for both tsunami events, with two goals in mind. The first goal is the validation of the method and the second is the comparison of the two displacement models. Some conclusions and remarks regarding the presented work are as follows:

Comparison of the numerical results with measurements from satellites and buoy data shows that the presented DG method can predict key features of the tsunamis such as the arrival time and sea surface heights accurately, with satisfactory agreements between numerical results and the data. Due to the good agreement with data and the high efficiency of the DG method, it is a suitable candidate for tsunami early warning systems for large-scale events.

The comparison of the static and dynamic source models shows that the impact of the dynamic approach on the near-field results is significant. Moreover, effects of the dynamic seabed displacement method on the water height can play a role in the far-field but only for waves with relatively small amplitudes. Therefore, an important factor in choosing the seabed displacement model includes how accurate results need to be and where the zone of interest lies with respect to the tsunami source. If the zone of interest is located near the source or if highly accurate results are needed, then the dynamic approach should be used. Moreover, the fault length and the rupture time have a big impact on this region. Based on the numerical results, long faults with long rupture times require an accurate dynamical source model.

In this work, we have only considered linear activation functions for the dynamic model but an examination of other rise functions or other dynamic source models is essential to understand the effects of the earthquake modeling on the tsunami results. Moreover, there is a lot of uncertainty in the source data and the bottom topography which may affect the accuracy of the numerical results.

Acknowledgements

References

[1]   M. Ulvrova, R. Paris, P. Nomikou, K. Kelfoun, S. Leibrandt, D. R. Tappin, and F. W. McCoy, "Source of the tsunami generated by the 1650 AD eruption of Kolumbo submarine volcano (Aegean Sea, Greece)," Journal of Volcanology and Geothermal Research, vol. 321, pp. 125–139, Jul. 2016.

[2]   M. de la Asunción, M. J. Castro, J. M. Mantas, and S. Ortega, "Numerical simulation of tsunamis generated by landslides on multiple GPUs," Advances in Engineering Software, vol. 99, pp. 59–72, Sep. 2016.

[3]   S.M. Ezzedine, I. Lomov, P.L. Miller, D.S. Dennison, D.S. Dearborn, and T.H. Antoun, "Simulation of asteroid impact on ocean surfaces, subsequent wave generation and the effect on US shorelines," Procedia Engineering, vol. 113, pp. 113-120, Jan. 2015.

[4]   B. Bonev, J.S. Hesthaven, F.X. Giraldo, and M.A. Kopera, "Discontinuous Galerkin scheme for the spherical shallow water equations with applications to tsunami modeling and prediction," Journal of Computational of Physics.

[5]   T. Saito and T. Furumura, "Three-dimensional simulation of tsunami generation and propagation: Application to intraplate events," Journal of Geophysical Research, vol. 114, no. B2, Feb. 2009.

[6]   Y. Oishi, M. D. Piggott, T. Maeda, S. C. Kramer, G. S. Collins, H. Tsushima, and T. Furumura, "Three-dimensional tsunami propagation simulations using an unstructured mesh finite element model," Journal of Geophysical Research: Solid Earth, vol. 118, no. 6, pp. 2998–3018, Jun. 2013.

[7] N. Mori, N. Yoneyama, and W. Pringle, "Effects of the Offshore Barrier Against the 2011 Off the Pacific Coast of Tohoku Earthquake Tsunami and Lessons Learned," Advances in Natural and Technological Hazards Research, pp. 121–132, Sep. 2014.

[8] T. Baba, S. Allgeyer, J. Hossen, P. R. Cummins, H. Tsushima, K. Imai, K. Yamashita, and T. Kato, "Accurate numerical simulation of the far-field tsunami caused by the 2011 Tohoku earthquake, including the effects of Boussinesq dispersion, seawater density stratification, elastic loading, and gravitational potential change," Ocean Modelling, vol. 111, pp. 46–54, Mar. 2017.

[9] T. Baba, N. Takahashi, Y. Kaneda, K. Ando, D. Matsuoka, and T. Kato, "Parallel Implementation of Dispersive Tsunami Wave Modeling with a Nesting Algorithm for the 2011 Tohoku Tsunami," Pure and Applied Geophysics, vol. 172, no. 12, pp. 3455–3472, Feb. 2015.

[10] R. Brecht, A. Bihlo, S. MacLachlan, and J. Behrens, "A well-balanced meshless tsunami propagation and inundation model," Advances in Water Resources, Dec. 2017.

[11] L. Rannabauer, M. Dumbser, and M. Bader, "ADER-DG with a-posteriori finite-volume limiting to simulate tsunamis in a parallel adaptive mesh refinement framework," Computers & Fluids, Feb. 2018.

[12] E. T. Flouri, N. Kalligeris, G. Alexandrakis, N. A. Kampanis, and C. E. Synolakis, "Application of a finite difference computational model to the simulation of earthquake generated tsunamis," Applied Numerical Mathematics, vol. 67, pp. 111–125, May 2013.

[13] X. Wang and P. L.-F. Liu, "Numerical simulations of the 2004 Indian Ocean tsunamis - coastal effects," Journal of Earthquake and Tsunami, vol. 01, no. 03, pp. 273–297, Sep. 2007.

[14] S. Clain, C. Reis, R. Costa, J. Figueiredo, M. A. Baptista, and J. M. Miranda, "Second-order finite volume with hydrostatic reconstruction for tsunami simulation," Journal of Advances in Modeling Earth Systems, vol. 8, no. 4, pp. 1691–1713, Oct. 2016.

[15] R. J. LeVeque, D. L. George, and M. J. Berger, "Tsunami modelling with adaptively refined finite volume methods," Acta Numerica, vol. 20, pp. 211–289, Apr. 2011.

[16] S. Takase, S. Moriguchi, K. Terada, J. Kato, T. Kyoya, K. Kashiyama, and T. Kotani, "2D–3D hybrid stabilized finite element method for tsunami runup simulations," Computational Mechanics, vol. 58, no. 3, pp. 411–422, May 2016.

[17] S. Blaise and A. St-Cyr, "A Dynamic hp-Adaptive Discontinuous Galerkin Method for Shallow-Water Flows on the Sphere with Application to a Global Tsunami Simulation," Monthly Weather Review, vol. 140, no. 3, pp. 978–996, Mar. 2012.

[18] S. Blaise, A. St-Cyr, D. Mavriplis, and B. Lockwood, "Discontinuous Galerkin unsteady discrete adjoint method for real-time efficient tsunami simulations," Journal of Computational Physics, vol. 232, no. 1, pp. 416–430, Jan. 2013.

[19] B. Seny, J. Lambrechts, T. Toulorge, V. Legat, and J.-F. Remacle, "An efficient parallel implementation of explicit multirate Runge–Kutta schemes for discontinuous Galerkin computations," Journal of Computational Physics, vol. 256, pp. 135–160, Jan. 2014.

[20] C. E. Castro, J. Behrens, and C. Pelties, "Optimization of the ADER-DG method in GPU applied to linear hyperbolic PDEs," International Journal for Numerical Methods in Fluids, vol. 81, no. 4, pp. 195–219, Oct. 2015.

[21] M. Asai, Y. Miyagawa, N. Idris, A. Muhari, and F. Imamura, "Coupled Tsunami Simulations Based on a 2D Shallow-Water Equation-Based Finite Difference Method and 3D Incompressible Smoothed Particle Hydrodynamics," Journal of Earthquake and Tsunami, vol. 10, no. 05, p. 1640019, Dec. 2016.

[22] M. Olabarrieta, R. Medina, M. Gonzalez, and L. Otero, "C3: A finite volume-finite difference hybrid model for tsunami propagation and runup," Computers & Geosciences, vol. 37, no. 8, pp. 1003–1014, Aug. 2011.

[23] E. Ortega, E. Oñate, S. Idelsohn, and C. Buachart, "An adaptive finite point method for the shallow water equations," International Journal for Numerical Methods in Engineering, vol. 88, no. 2, pp. 180–204, Apr. 2011.

[24] S. M. Reckinger, O. V. Vasilyev, and B. Fox-Kemper, "Adaptive wavelet collocation method on the shallow water model," Journal of Computational Physics, vol. 271, pp. 342–359, Aug. 2014.

[25] Y. Yamazaki, T. Lay, K. F. Cheung, H. Yue, and H. Kanamori, "Modeling near-field tsunami observations to improve finite-fault slip models for the 11 March 2011 Tohoku earthquake," Geophysical Research Letters, vol. 38, no. 7, p. n/a–n/a, Apr. 2011.

[26] A. Suppasri, F. Imamura, and S. Koshimura, "Effects of the Rupture Velocity of Fault Motion, Ocean Current and Initial Sea Level on the Transoceanic Propagation of Tsunami," Coastal Engineering Journal, vol. 52, no. 2, pp. 107–132, Jun. 2010.

[27] D. Dutykh and F. Dias, "Tsunami generation by dynamic displacement of sea bed due to dip-slip faulting," Mathematics and Computers in Simulation, vol. 80, no. 4, pp. 837–848, Dec. 2009.

[28] Y. Yamazaki, K. F. Cheung, and Z. Kowalik, "Depth-integrated, non-hydrostatic model with grid nesting for tsunami generation, propagation, and run-up," International Journal for Numerical Methods in Fluids, vol. 67, no. 12, pp. 2081–2107, Dec. 2010.

[29] D. Dutykh, D. Mitsotakis, X. Gardeil, and F. Dias, "On the use of the finite fault solution for tsunami generation problems," Theoretical and Computational Fluid Dynamics, vol. 27, no. 1–2, pp. 177–199, Mar. 2012.

[30] T. Ohmachi, "Simulation of Tsunami Induced by Dynamic Displacement of Seabed due to Seismic Faulting," Bulletin of the Seismological Society of America, vol. 91, no. 6, pp. 1898–1909, Dec. 2001.

[31] Y. Ohta, T. Kobayashi, H. Tsushima, S. Miura, R. Hino, T. Takasu, H. Fujimoto, T. Iinuma, K. Tachibana, T. Demachi, T. Sato, M. Ohzono, and N. Umino, "Quasi real-time fault model estimation for near-field tsunami forecasting based on RTK-GPS analysis: Application to the 2011 Tohoku-Oki earthquake (Mw9.0)," Journal of Geophysical Research: Solid Earth, vol. 117, no. B2, p. n/a–n/a, Feb. 2012.

[32] C. J. Vogl and R. J. LeVeque, "A High-Resolution Finite Volume Seismic Model to Generate Seafloor Deformation for Tsunami Modeling," Journal of Scientific Computing, vol. 73, no. 2–3, pp. 1204–1215, May 2017.

[33] C. Uphoff, S. Rettenberger, M. Bader, E. H. Madden, T. Ulrich, S. Wollherr, and A.-A. Gabriel, "Extreme scale multi-physics simulations of the tsunamigenic 2004 sumatra megathrust earthquake," Proceedings of the International Conference for High Performance Computing, Networking, Storage and Analysis on - SC '17, 2017.

[34] F. X. Giraldo, J. S. Hesthaven, and T. Warburton, "Nodal High-Order Discontinuous Galerkin Methods for the Spherical Shallow Water Equations," Sep. 2002.

[35] S. Gottlieb, D. Ketcheson, and C.-W. Shu, "Strong Stability Preserving Runge-Kutta and Multistep Time Discretizations," Jan. 2011.

[36] Y. Xing, X. Zhang, and C.-W. Shu, "Positivity-preserving high order well-balanced discontinuous Galerkin methods for the shallow water equations," Advances in Water Resources, vol. 33, no. 12, pp. 1476–1493, Dec. 2010.

[37] Y. Okada, "Surface deformation due to shear and tensile faults in a half-space," Bulletin of the Seismological Society of America, vol. 75, no. 4, p. 1135-1154, Aug. 1985.

[38] A. Kundu, Ed., "Tsunami and Nonlinear Waves," 2007.

[39] G. Shao, X. Li, C. Ji, and T. Maeda, "Focal mechanism and slip history of the 2011 M w 9.1 off the Pacific coast of Tohoku Earthquake, constrained with teleseismic body and surface waves," Earth, Planets and Space, vol. 63, no. 7, pp. 559–564, Jul. 2011.

[40] National Oceanic and Atmospheric Administration (2005), Deep-Ocean Assessment and Reporting of Tsunamis (DART(R)), National Centers for Environmental Information, NOAA, 2017.

[41] K. Hirata, K. Satake, Y. Tanioka, T. Kuragano, Y. Hasegawa, Y. Hayashi, and N. Hamada, "The 2004 Indian Ocean tsunami: Tsunami source model from satellite altimetry," Earth, Planets and Space, vol. 58, no. 2, pp. 195–201, Feb. 2006.

[42] D. Gopinathan, M. Venugopal, D. Roy, K. Rajendran, S. Guillas, and F. Dias, "Uncertainties in the 2004 Sumatra–Andaman source through nonlinear stochastic inversion of tsunami waves," Proceedings of the Royal Society A: Mathematical, Physical and Engineering Science, vol. 473, no. 2205, p. 20170353, Sep. 2017.

[43] Y. Fujii and K. Satake, "Tsunami Source of the 2004 Sumatra-Andaman Earthquake Inferred from Tide Gauge and Satellite Data," Bulletin of the Seismological Society of America, vol. 97, no. 1A, pp. S192–S207, Jan. 2007.

[44] C. J. Ammon, "Rupture Process of the 2004 Sumatra-Andaman Earthquake," Science, vol. 308, no. 5725, pp. 1133–1139, May 2005.

[45] M. Chlieh, J.-P. Avouac, V. Hjorleifsdottir, T.-R. A. Song, C. Ji, K. Sieh, A. Sladen, H. Hebert, L. Prawirodirdjo, Y. Bock, and J. Galetzka, "Coseismic Slip and Afterslip of the Great Mw 9.15 Sumatra-Andaman Earthquake of 2004," Bulletin of the Seismological Society of America, vol. 97, no. 1A, pp. S152–S173, Jan. 2007.

[46] J. Rhie, D. Dreger, R. Burgmann, and B. Romanowicz, "Slip of the 2004 Sumatra-Andaman Earthquake from Joint Inversion of Long-Period Global Seismic Waveforms and GPS Static Offsets," Bulletin of the Seismological Society of America, vol. 97, no. 1A, pp. S115–S127, Jan. 2007.

[47] B. Poisson, C. Oliveros, and R. Pedreros, "Is there a best source model of the Sumatra 2004 earthquake for simulating the consecutive tsunami?," Geophysical Journal International, vol. 185, no. 3, pp. 1365–1378, Apr. 2011.

[48] Scharroo, R., E. W. Leuliette, J. L. Lillibridge, D. Byrne, M. C. Naeije, and G. T. Mitchum, RADS: Consistent multi-mission products, in Proc. of the Symposium on 20 Years of Progress in Radar Altimetry, Venice, 20-28 September 2012, Eur. Space Agency Spec. Publ., ESA SP-710, p. 4 pp., 2013.